

Full length article

Extreme reduction of thermal conductivity by embedding Al₂O₃ nanoparticles into single-crystalline Bi nanowires



Jong Wook Roh^a, Jinhee Ham^b, Jeongmin Kim^a, Hongjae Moon^a, Hyun Sik Kim^c,
Wooyoung Lee^{a,*}

^a Department of Materials Science and Engineering Yonsei University, 50 Yonsei-ro, Seodaemun-gu, Seoul 03722, Republic of Korea

^b Agency for Defense Development, Yuseong P.O. Box 35, Daejeon 34186, Republic of Korea

^c Inorganic Materials Lab, Samsung Advanced Institute of Technology, Samsung Electronics, 130 Samsung-ro, Suwon-si 16678, Republic of Korea

ARTICLE INFO

Article history:

Received 11 June 2017

Accepted 8 July 2017

Available online 9 July 2017

Keywords:

Bismuth

Nanowires

Nanoparticles

Thermal conductivity

Phonon scattering

ABSTRACT

Al₂O₃ nanoparticles-embedded single-crystalline Bi nanowires were successfully synthesized without using any templates via the spontaneous growth of Bi thin films covered with Al₂O₃ nanoparticles. It is experimentally confirmed that Al₂O₃ nanoparticles were embedded into the single-crystalline Bi nanowires by using the high-resolution transmission electron microscopy and energy dispersive X-ray spectrometry. The temperature-dependent thermal conductivities of individual Al₂O₃ nanoparticles-embedded single-crystalline Bi nanowires were measured directly using suspended micro-devices. The thermal conductivities of the Al₂O₃ nanoparticles-embedded Bi nanowires were found to be extremely low compared with those of pure Bi nanowires of similar diameters. Moreover, the thermal conductivity of the Al₂O₃ nanoparticles-embedded Bi nanowires was not size-dependent, i.e., it did not vary for nanowires with significantly different diameters. This result suggests that the phonon-boundary scattering is not the dominant phonon scattering mechanism in these systems while the phonon-boundary scattering is dominant in the pure single-crystalline nanowires. From the experimental measurements and theoretical calculation, these drastic reduction and unique tendency in the thermal conductivities of Al₂O₃ nanoparticles-embedded Bi nanowires were explained by the combined effect of the phonon-boundary scattering and impurity scattering occurring between the embedded Al₂O₃ nanoparticles and Bi matrix.

© 2017 Acta Materialia Inc. Published by Elsevier Ltd. All rights reserved.

1. Introduction

Over the past few decades, thermoelectric energy conversion systems that convert thermal energy into electrical energy or vice versa have increasingly attracted attention in the context of power generation and cooling systems. To increase the efficiency of thermoelectric devices for widening the range of practical applications, most of the researches have been mainly focused on improving the figure of merit (ZT) of the thermoelectric materials; it is expressed as $ZT = S^2\sigma T/\kappa$, where S , σ , κ , and T are the Seebeck coefficient, electrical conductivity, thermal conductivity, and absolute temperature, respectively. However, the trade-off requirement between S , σ , and κ in bulk materials leads to a low ZT , implying that the thermoelectric efficiency in bulk materials is limited. However,

since the effectiveness of phonon scattering in reducing the lattice thermal conductivity without decreasing the electrical properties was established, use of nanostructures in thermoelectric materials has widely been studied [1–3]. Several researches have reported that nanocomposite materials are able to achieve this owing to the introduction of more interfaces [4–9]. Kim et al. [7] demonstrated that by using In_{0.53}Ga_{0.47}As containing ErAs nanoparticles (NPs) the thermal conductivity was decreased by a factor of 2 below the alloy limit without degradation of the crystal structure. A combined theoretical and experimental study revealed that the ErAs NPs dispersed in the host materials effectively scattered mid-to-long-wavelength phonons, whereas the atomic scale defects in the host materials mainly scattered the Brillouin zone edge phonons. Zhao et al. [10] also reported that nano-SiC dispersed within synthesized Bi₂Te₃ reduced the lattice thermal conductivity of the alloy. He et al. [11] achieved a ZT improvement of 11% by reducing the lattice thermal conductivity through the introduction of

* Corresponding author.

E-mail address: wooyoung@yonsei.ac.kr (W. Lee).

insulating ZrO_2 nanopowders into the CoSb_3 matrix.

Furthermore, Hicks et al. [12,13] have reported that the three parameters S , σ , and κ can be controlled independently owing to the quantum confinement and size effects. A few studies have been conducted on thermal transport in individual nanowires (NWs), showing that the thermal conductivity was reduced by the phonon scattering at the boundary surface [14–16]. In particular, Bi NWs have attracted noticeable attention because of their unique electrical and thermal transport phenomena [17–20]. Bi has a relatively long phonon mean free path of 11–14 nm at 300 K, predicted from the Dulong–Petit limit and $\ell \sim 3\kappa/(C_v \times v)$, where κ is the measured thermal conductivity of bulk Bi (8–10 W/m·K), C_v is the volumetric specific heat of bismuth ($\sim 1.2 \text{ J/cm}^3 \cdot \text{K}$), and v is the speed of sound ($\sim 1790 \text{ m/s}$). Based on the phonon mean free path of Bi, it was expected that the thermal conductivity of Bi NWs could be decreased by the boundary scattering of the heat carriers when their diameter was similar to the mean free path of the heat carriers including contributions from both phonons and electrons. In prior works, it was experimentally shown that the thermal conductivities of single-crystalline Bi NWs and Bi–Te core/shell NWs were effectively reduced by the scattering of the heat carriers at the boundary surface and rough interface, respectively [17,21,22]. Considering these studies, it can be expected that the thermal conductivities may be drastically suppressed by a combined effect of the nano-inclusions and boundary scattering in NWs with nanocomposite structures. However, despite the importance of understanding the heat transport mechanism in nanoscale materials, there has been no systematic investigation on the thermal transport phenomena in NWs with nanocomposite structures. Herein, we demonstrate a facile synthesis of Al_2O_3 nanoparticles-embedded single-crystalline Bi NWs using the on-film formation of nanowires (OFF-ON) method and report extremely low thermal conductivities for the Al_2O_3 nanoparticles-embedded Bi NWs owing to the combined effect of the phonon-boundary scattering at the surface and phonon-interface scattering between the embedded Al_2O_3 NPs and Bi matrix.

2. Experimental

2.1. Materials

In this work, Al_2O_3 nanopowders (Aluminum oxide, nanopowder, 13 nm primary particle size, 99.8%, SIGMA-ALDRICH) were utilized. Prior to the synthesis of NWs, the Al_2O_3 NPs were purified to remove the organic contaminations by stirring and sonication using acetone, ethanol, and deionized (D. I.) water. D. I. water was obtained by an 18-M Ω system.

2.2. Synthesis of Al_2O_3 nanoparticles-embedded Bi nanowires

Fig. 1 schematically illustrates the OFF-ON process for the synthesis of the Al_2O_3 NPs-embedded Bi NWs, explaining the origin and driving force for their spontaneous growth. At first, the D. I. water containing the purified Al_2O_3 NPs is spun onto the surface of a thermally oxidized Si (100) substrate using a spin-coater. Then, a Bi thin film is deposited on the layer of Al_2O_3 NPs at a deposition rate of 44 Å/s using an ultra-high vacuum radio frequency (UHV-RF) sputtering system with a base pressure of 4×10^{-8} torr. To initiate the incompatibility of the thermal expansion between the films and SiO_2/Si substrate, the Bi thin film-deposited substrate is annealed at 270 °C for 12 h in vacuum at a pressure lower than 1.0×10^{-3} torr. The thermal mismatch between the films and SiO_2/Si substrate is attributed to the large difference between the thermal expansion coefficients of Bi ($13.4 \times 10^{-6}/^\circ\text{C}$) and SiO_2/Si ($0.5 \times 10^{-6}/^\circ\text{C}$ – $2.4 \times 10^{-6}/^\circ\text{C}$). This difference between the thermal expansion

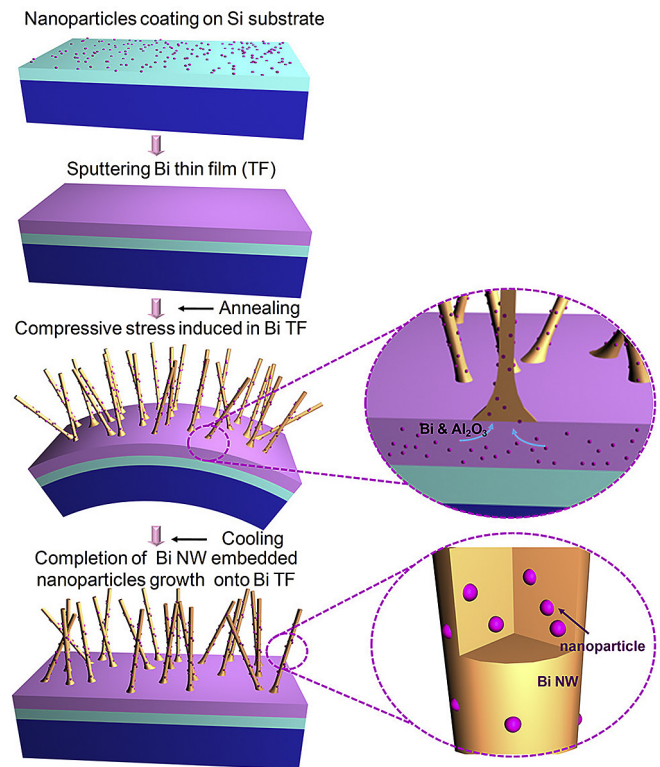


Fig. 1. Schematic of the growth mechanism of the Al_2O_3 nanoparticles-embedded Bi nanowires by the OFF-ON process. First, the Al_2O_3 NPs are spun on an oxidized Si (100) substrate. Then, a Bi thin film is deposited on the layer of Al_2O_3 NPs by sputtering. To initiate the incompatibility between the thermal expansion of the films and Si/SiO_2 substrate, the Bi thin film-deposited substrate is annealed. The Bi thin film expands during annealing. On cooling the growth of Al_2O_3 nanoparticles-embedded Bi nanowires is completed.

coefficients provided the thermodynamic driving force for the spontaneous growth during the thermal annealing process. The Bi thin film expands during annealing, and the SiO_2/Si substrate limits this expansion. More details on the growth mechanism by the OFF-ON method can be found in the literature [18,22].

2.3. Investigation of microstructures

Field emission scanning electron microscope (FE-SEM) images were obtained by JEOL JSM-6700F. The microstructures and elemental analysis of Al_2O_3 NPs-embedded Bi NWs were analyzed via scanning transmission electron microscopy (STEM, JEM-2100F and JEM-2011HC, JEOL) at an accelerating voltage of 200 kV and energy dispersive X-ray spectrometry (EDS, INCA X-sight 7421, Oxford Instruments), respectively.

2.4. Device fabrication and characterization of thermal properties

Suspended micro-devices consisting of two adjacent low-stress silicon nitride (SiN_x) membranes ($25 \times 35 \mu\text{m}$) were utilized to investigate the thermal conductivities of the individual Al_2O_3 NPs-embedded Bi NWs. Two membranes of the micro-devices were suspended with five long SiN_x beams with a length and width of 400 μm and 2 μm , respectively. On each membrane, a Pt resistance thermometer (PRT) coil with a width of 800 nm and thickness of 30 nm, simultaneously acting as a heater and thermometer, was patterned. For the thermal conductivity measurement, an Al_2O_3 NPs-embedded Bi individual NW was placed between the two suspended membranes via a drop-casting method. Subsequently, a

Pt/C composite was deposited locally, to improve the thermal contact between the NW and two membranes, using an electron beam of a dual-beam focused ion beam (FIB) system (FEI Quanta 3D FEG). An electron beam with a low accelerating voltage of 2 kV and 50 pA was utilized to avoid damaging the Bi NW during the Pt/C thermal contact fabrication process. A more detailed description of the thermal conductivity measurement using these suspended devices is presented in prior works [14–17]. A direct current (DC) generated from a data acquisition (DAQ) board, was applied to the PRT coils patterned on the heating membranes coupled with an alternating current (AC) generated from a lock-in amplifier (Stanford Research Systems, Model: SR 850) after engaging the suspended micro-devices inside a closed cycle cryostat. The DC resulted in Joule heat ($Q_h = I^2 R_h$) generation, and consequently increased the temperature of the heating membrane (T_h), where I and R_h are the applied current and resistance of the PRT coil on the heating membrane, respectively. A certain amount of heat generated by the PRT coil on the heating membrane was transported to the sensing membrane through an individual NW with a negligible heat loss. Heat conduction via the NW allowed the temperature of the sensing membrane (T_s) to also increase. These changes in the temperatures T_h and T_s in each membrane were measured using the variation of the AC resistance of the PRT coil on each membrane, enabling the calculation of thermal conductance.

2.5. Method of thermal conductivity calculation

Total thermal conductivity (κ_{total}) is the sum of lattice thermal conductivity (κ_l), heat transported by electrons (κ_e) and holes (κ_h), and contribution from bipolar diffusion (κ_{bp}). Except κ_l , computation of the thermal conductivity owing to charged carriers (κ_e , κ_h , and κ_{bp}) requires band parameters of both the conduction and valence bands of the material. The transport measurements required to acquire the band parameters of Bi NWs are scarce in the literature; therefore, we have instead used the experimental results corresponding to Bi single-crystals reported by Gallo et al. [23]. From these band parameters, κ_e , κ_h , and κ_{bp} were calculated [24]. κ_l was calculated from the Debye–Callaway model. The Debye–Callaway model is a simplified version of the original Callaway model where it is assumed that the phonon group velocity is constant. Further details regarding κ_l calculation can be found in Ref. [25].

3. Results and discussion

3.1. Microstructure of Al_2O_3 NPs-embedded Bi NWs

The as-grown Al_2O_3 NPs-embedded Bi NWs are found to be uniform and straight with aspect ratios exceeding 1000, as shown in Fig. 2(a). The NW grown is from the surface of the as-sputtered films containing the Al_2O_3 NPs. Substantial atomic diffusion occurs owing to the compressive stress at the interface between the substrate and Bi films containing the Al_2O_3 NPs. It should be noted that the annealing temperature during the synthesis was similar to the melting point of Bi (~ 271 °C) [18]. Consequently, the spontaneous growth of the Al_2O_3 NPs-embedded Bi nanowires is a way of releasing the compressive stress through atomic diffusion near the pinned grain boundaries. This diffusion of Bi atoms enables the Al_2O_3 NPs to diffuse into the NWs as illustrated in Fig. 1. Fig. 2(b) shows that the surfaces of the NWs have a roughness that is caused by the Al_2O_3 NPs diffused into the NWs during the growth process. For the analysis of the elemental distribution of the Al_2O_3 NPs-embedded NWs, an EDS elemental line-scan profile was performed across an approximately 70 nm-thick NW along the arrow shown in Fig. 2(b). Fig. 2(c) shows the homogeneous

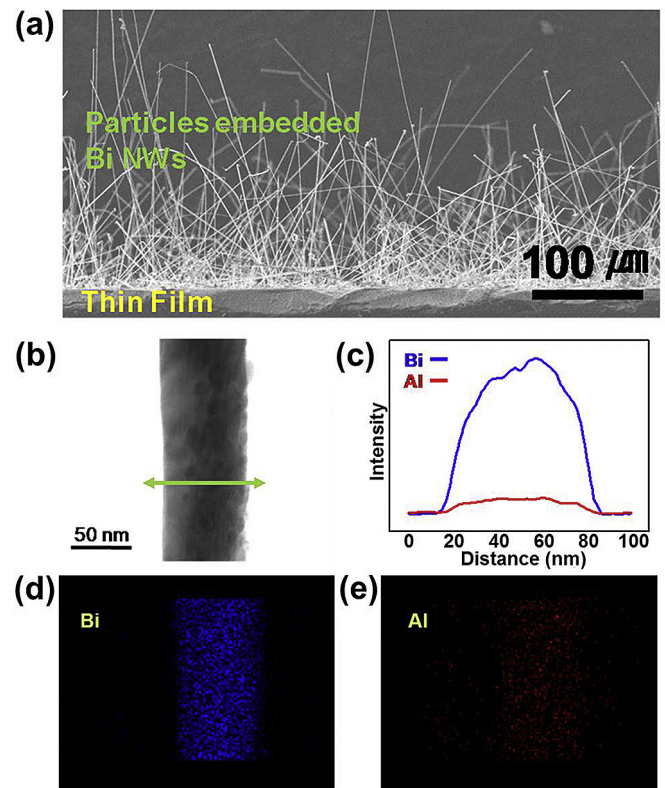


Fig. 2. (a) FE-SEM image and (b) STEM image of the Al_2O_3 NPs-embedded Bi NWs (c) Elemental profile measured along the arrow shown in (b). (d and e) The corresponding Bi (blue) and Al (red) maps obtained via energy dispersive X-ray spectrometry. The as-grown Al_2O_3 NPs-embedded Bi NWs are uniform and straight. The surfaces NWs have a roughness caused by the Al_2O_3 NPs diffused into the NWs during the growth process. The Al_2O_3 NPs are diffused and embedded in the Bi NWs by the OFF-ON method. (For interpretation of the references to colour in this figure legend, the reader is referred to the web version of this article).

distribution of Al (red line) in the Bi matrix (blue line) across the radial direction, clearly indicating that the Al_2O_3 NPs are diffused and embedded in the Bi NWs by the OFF-ON method. The corresponding EDS elemental mapping images (Fig. 2(d) and (e)) further show the spatial distribution of Al and Bi elements, supporting that the Al_2O_3 NPs are dispersed over the entire surface of the Bi NWs.

For obtaining a direct evidence of the Al_2O_3 NPs being embedded in the single-crystalline Bi matrix of the NWs, the high-resolution transmission electron microscopy (HR-TEM) coupled with selected area electron diffraction (SAED) was employed. The sample for the TEM investigation was prepared using the dual-beam FIB system, as displayed in Fig. 3. The HR-TEM image and electron diffraction data in Fig. 4 further confirm the existence of embedded Al_2O_3 NPs in the single-crystalline Bi matrix. The atomic mismatch in the yellow circle in Fig. 4 provides evidence that the other element is embedded in the Bi matrix. The diameter of the atomic mismatch area is measured to be approximately 10–15 nm that is similar to the diameter of the Al_2O_3 NPs used in this experiment. The corresponding SAED pattern of the yellow circle (area a) reveals that the Bi NWs grow along the [110] direction with the Al_2O_3 NPs (inset of Fig. 4). The bright-field TEM image in Fig. 5(a) reveals that the NPs have a circular shape and are single-crystalline. The corresponding EDX point analysis in Fig. 5(b) clearly shows that elemental Al is detected in the corresponding area of the Al_2O_3 NPs in Fig. 5(a), while Bi is only found in the matrix. This implies that the Al_2O_3 NPs diffuse in the Bi matrix

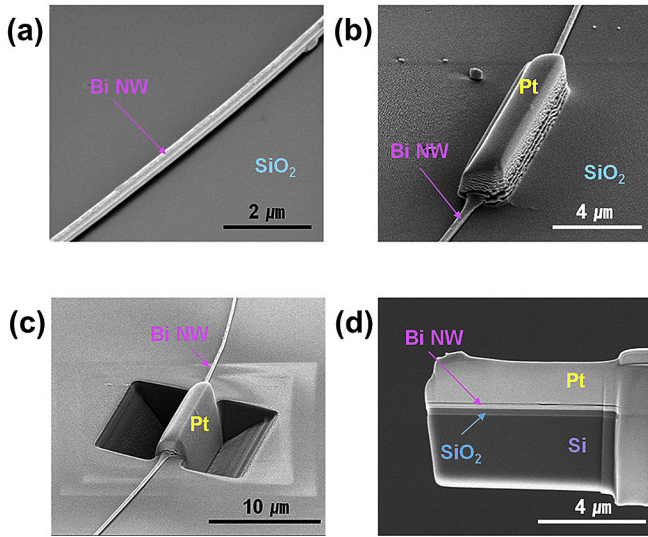


Fig. 3. SEM images of the sample-preparation process for the TEM investigation. (a) Al_2O_3 NPs-embedded Bi NWs on the SiO_2/Si substrate. (b) Deposition of Pt/C passivation layer using an electron beam of the dual-beam FIB system. (c) Cutting the substrate around the TEM sample containing the Bi NWs using an ion beam of the dual-beam FIB system. (d) Fabricated TEM sample containing the Al_2O_3 NPs-embedded Bi NWs.

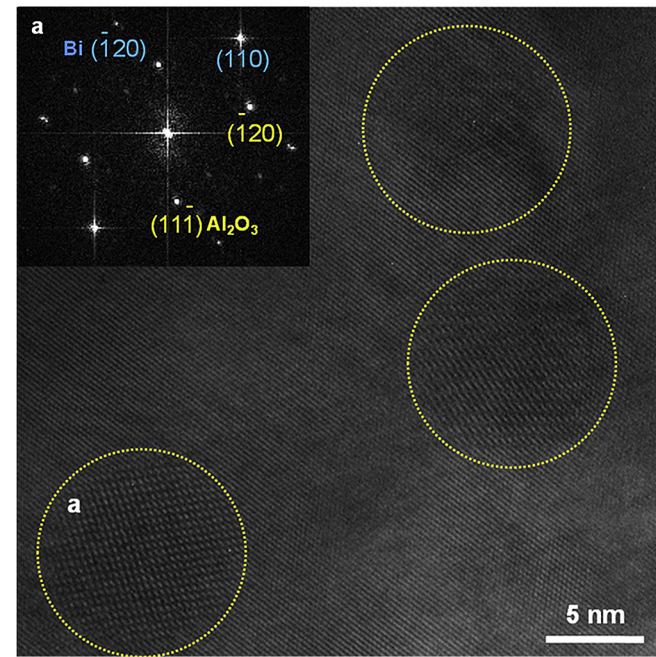


Fig. 4. HR-TEM image and the corresponding SAED image of the Al_2O_3 NPs-embedded Bi NWs (inset). The inset shows that the Bi NWs grow along the $[110]$ direction with the Al_2O_3 NPs. The atomic mismatch in the yellow circles provides evidence that the Al_2O_3 NPs are embedded in the Bi matrix. (For interpretation of the references to colour in this figure legend, the reader is referred to the web version of this article).

along with the Bi atom diffusion during the synthesis of the NWs using the OFF-ON method.

3.2. Effective phonon scattering in the Al_2O_3 NPs-embedded Bi NWs

Fig. 6(a) shows a FE-SEM image of a suspended micro-device that consists of two adjacent silicon nitride (SiN_x) membranes

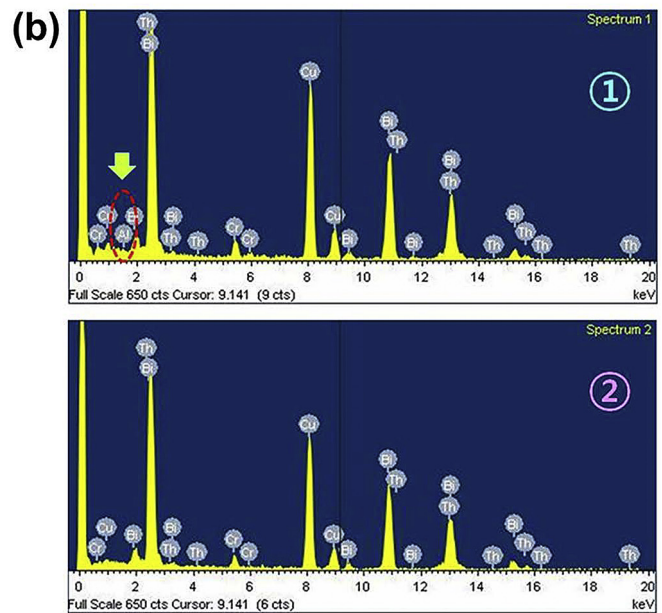
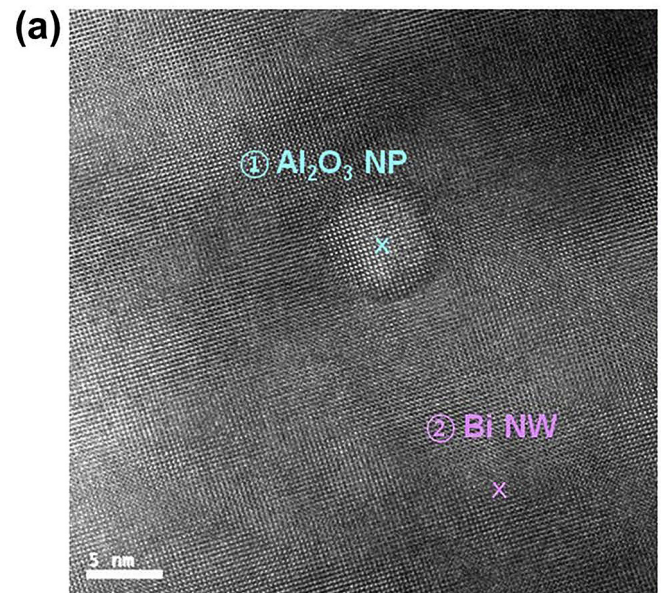


Fig. 5. (a) TEM image of the Al_2O_3 NPs-embedded Bi NWs and (b) the corresponding result of the point EDS analysis. The NPs have a circular shape and are single-crystalline. Elemental Al is detected in the corresponding area of the Al_2O_3 NPs in (a), while Bi is only found in the matrix.

that are suspended with five long SiN_x beams. All the thermal conductivity (κ) measurements were conducted via a closed cycle cryostat under high vacuum and pressure less than 5×10^{-6} torr to eliminate the heat convection noise. Owing to the suspended micro-devices and Pt/C thermal contact, the NW is the only pathway for thermal conduction from the heating membrane to sensing membrane. For examining the thermal contact resistance of the Pt/C thermal contact, it was fabricated twice before and after the first thermal conductivity measurement, and its thermal conductivity was compared to the single contact case. The second thermal contact was similar to the previous one in size; therefore, the total area doubled as shown in Fig. 6(b). Fig. 6(c) shows the measured thermal conductivities of the Al_2O_3 NPs-embedded Bi NWs with a diameter (d) of 310 nm in the temperature range from

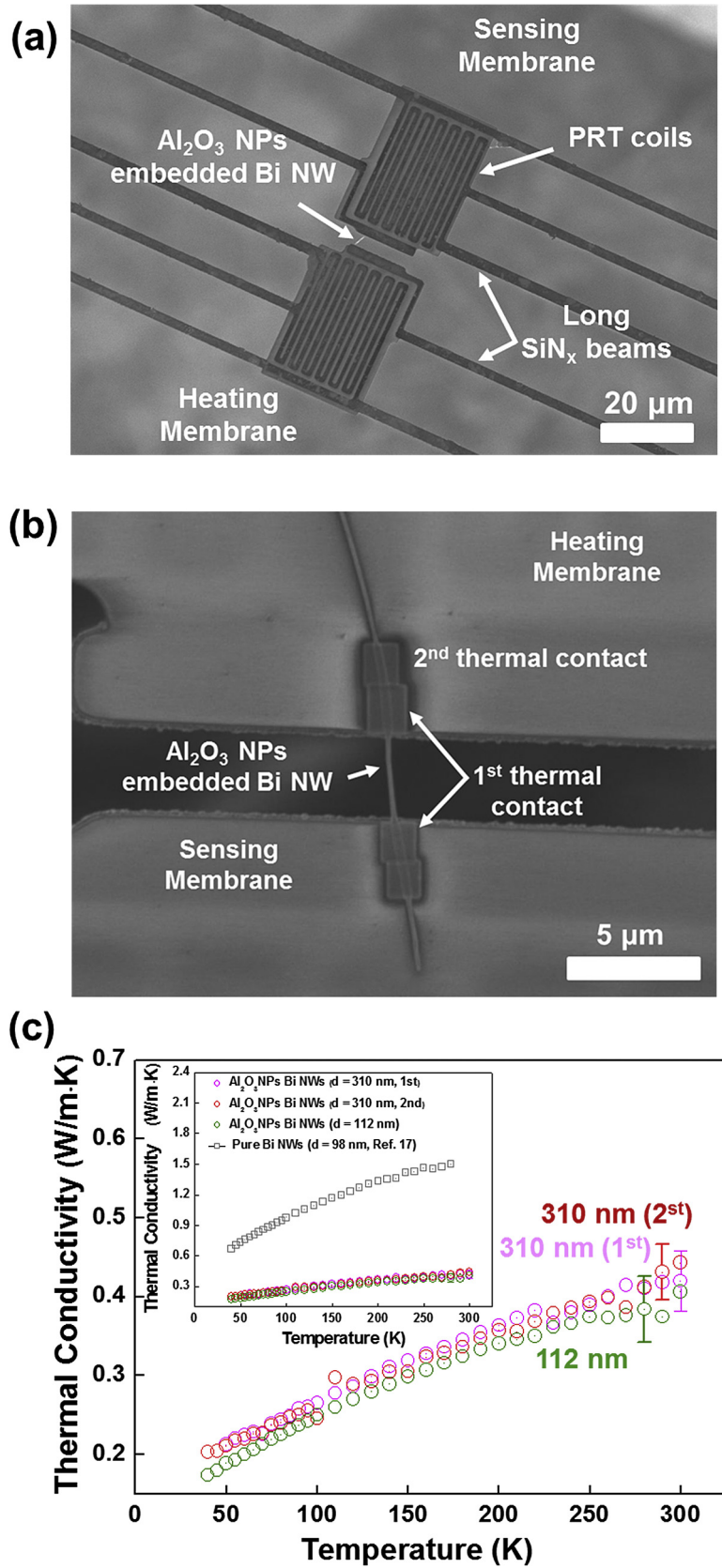


Fig. 6. (a) FE-SEM image of the suspended micro-devices (b) FE-SEM image of an individual Al_2O_3 NPs-embedded Bi NW on the membranes after formation of the second thermal contact. (c) Measured thermal conductivities of individual Al_2O_3 NPs-embedded Bi NWs with $d = 112$ and 310 nm. The inset shows the thermal conductivity of pure Bi nanowires with $d = 98$ nm. In (a), owing to the suspended micro-devices and Pt/C thermal contact, the NW is the only pathway for thermal conduction from the heating membrane to sensing membrane. The second thermal contact is similar to the previous one in size; therefore, the total area is doubled in (b). (c) exhibits a monotonic decrease in the thermal conductivity with decreasing temperature. The thermal conductivities of the Al_2O_3 NPs-embedded Bi NWs are much lower than those of single-crystalline bulk Bi and Bi NWs of a similar diameter.

40 to 340 K before and after the fabrication of the second thermal contact. Fig. 6(c) displays that there is almost no change in the thermal conductivity of the 310-nm NW after the formation of the additional thermal contact. The maximum difference between the thermal conductivities is less than 0.03 W/m·K in the measured temperature range, equivalent to a maximum ratio of thermal conductivity difference of less than 7%. This result indicates that the thermal contact resistance of the Pt/C thermal contact is negligible despite the significantly low total thermal conductivity.

Fig. 6(c) exhibits a monotonic decrease in the thermal conductivity with decreasing temperature. The measured thermal conductivity of the Al₂O₃ NPs-embedded Bi NWs with $d = 310$ nm is ~0.44 W/m·K at room temperature. The thermal conductivities of the Al₂O₃ NPs-embedded Bi NWs are much lower than not only those of single-crystalline bulk Bi, but also of single-crystalline Bi NWs of a similar diameter. It is to be noted that in our previous work the thermal conductivity of pure Bi NWs with a diameter of 98 nm grown using the OFF-ON method was measured to be ~1.6 W/m·K at room temperature [17]. This clearly indicates the occurrence of strong phonon scattering in the Al₂O₃ NPs-embedded Bi NWs. We also find that the temperature dependence of the thermal conductivity of the Al₂O₃ NPs-embedded Bi NWs is different compared to that of bulk Bi. While the thermal conductivity of bulk Bi has a sharp peak at 4 K, that of the Al₂O₃ NPs-embedded Bi NWs with a diameter of 310 nm and 112 nm does not exhibit any peak in the temperature range that is considered, suggesting that this peak-shift is caused by the enhanced boundary scattering of phonons.

Although the phonon-boundary scattering at the NW surface generally one of the reason for the suppression of the thermal transport in NW system, it should be noted that the thermal conductivity is not size-dependent, i.e., it has similar values for NWs with significantly different diameters as shown in Fig. 6(c). However, according to our previous work, for a NW system, the thermal conductivity should decrease with a decrease in the diameter of the NWs owing to the enhanced phonon-boundary scattering. This result suggests that the phonon-boundary scattering is not the dominant phonon scattering mechanism in the Al₂O₃ NPs-embedded Bi NWs. Kim et al. [7] have demonstrated that ErAs NPs scatter mid-to-long-wavelength phonons, while atomic scale defects in the InGaAs matrix effectively scatter the Brillouin zone edge phonons. Analogously, long-wavelength phonons are expected to be effectively scattered by the Al₂O₃ NPs embedded in the Bi NWs. Moreover, the mean free path of the phonons at 300 K is predicted to be approximately 11–14 nm, similar to the diameter of the Al₂O₃ NPs, suggesting that the thermal conductivity probably decreases because of the embedded Al₂O₃ NPs. Consequently, the combination effects of phonon-boundary scattering and impurity scattering of the long-wavelength phonons suppressed the thermal conductance via the Al₂O₃ NPs-embedded Bi NW, resulting in an extremely low thermal conductivity. Additionally, the modification of the acoustic impedance due to the different atomic masses between the NPs and Bi matrix could play a significant role in the

reduction of thermal conductivity. Liu et al. [26] reported a similar result of a large reduction in the thermal conductivity of the Ge quantum dot superlattice caused by the acoustic impedance mismatch between Si and Ge.

3.3. Theoretical study using thermal conductivity modeling

κ_l can be calculated as shown in Eq. (1) where C , v , τ_{total} , and ω are the heat capacity, phonon velocity, total relaxation time, and frequency, respectively.

$$\kappa_l = \frac{1}{3} \int C(\omega)v^2(\omega)\tau_{\text{total}}(\omega)d\omega. \quad (1)$$

From the Debye–Callaway equation, κ_l in Eq. (1) can be approximated to

$$\kappa_l = \frac{k_B}{2\pi^2v} \left(\frac{k_B T}{\hbar} \right)^3 \int_0^{\theta_a/T} \frac{\tau_{\text{total}}(z)z^4 e^z}{(e^z - 1)^2} dz, \quad (2)$$

where k_B , \hbar , θ_a , and z are the Boltzmann constant, reduced Planck's constant, Debye temperature, and $\hbar\omega/k_B T$, respectively. Once the τ_{total} is calculated from $\tau_{\text{total}}(z)^{-1} = \sum_i \tau_i(z)^{-1}$, where τ_i are the individual relaxation times for different scattering, modeling κ_l using Eq. (2) becomes straightforward. Table 1 shows the individual relaxation times chosen for the different samples. For example, for single-crystal bulk Bi [23], only the Umklapp scattering and boundary scattering are used. The relaxation rate for the Umklapp scattering (τ_U^{-1}) is expressed as

$$\tau_U^{-1} = A_N \frac{2}{(6\pi^2)^{1/3}} \frac{k_B V^{1/3} \gamma^2 \omega^2 T}{M v^3}, \quad (3)$$

where V , γ , M , and A_N are the atomic volume, Grüneisen parameter, average atomic mass, and the free parameter that takes the momentum-conserving normal scattering into account, respectively. Except A_N , all the other parameters were found from the literature for Bi.

The relaxation rate for the boundary scattering (τ_B^{-1}),

$$\tau_B^{-1} = \frac{v}{d}, \quad (4)$$

is the ratio of the phonon velocity (v) to the size of the boundary (d). For single-crystal bulk Bi, we have assumed its boundary to be the sample surface ($d = 1$ mm). By fitting Eq. (2) to the experimental data, we found that $A_N = 8$ (Table 1) described the data satisfactorily (Fig. 7). For the Bi NW (98 nm) sample [17], while keeping A_N the same as that used for bulk Si, we only added the impurity scattering term ($\propto \omega^4$) to take into account the thin oxide layer formed on the surface of the Bi NW (Fig. 7) [20].

When we embed Al₂O₃ NPs in the surface of the Bi NW, we expect an additional impurity scattering from the Al₂O₃ NPs.

Table 1

Contributions to the total relaxation rate (τ_{total}^{-1}) used to compute κ_l of bulk Bi, Bi NWs (98 nm), and Al₂O₃ NPs-embedded Bi NWs (310 nm and 112 nm).

Sample	τ_{total}^{-1}	A_N	C_i (s ³)
Bulk Bi	$A_N \tau_U^{-1} + \tau_{B(d=1\text{mm})}^{-1}$	8	—
Bi NW (98 nm)	$A_N \tau_U^{-1} + \tau_{B(d=98\text{nm})}^{-1} + C_i \omega^4$	8	1.36E-40
Al ₂ O ₃ NPs-embedded Bi NWs (310 nm)	$A_N \tau_U^{-1} + \tau_{B(d=310\text{nm})}^{-1} + C_i \omega^4$	8	6.81E-40
Al ₂ O ₃ NPs-embedded Bi NWs (112 nm)	$A_N \tau_U^{-1} + \tau_{B(d=112\text{nm})}^{-1} + C_i \omega^4$	8	6.81E-40

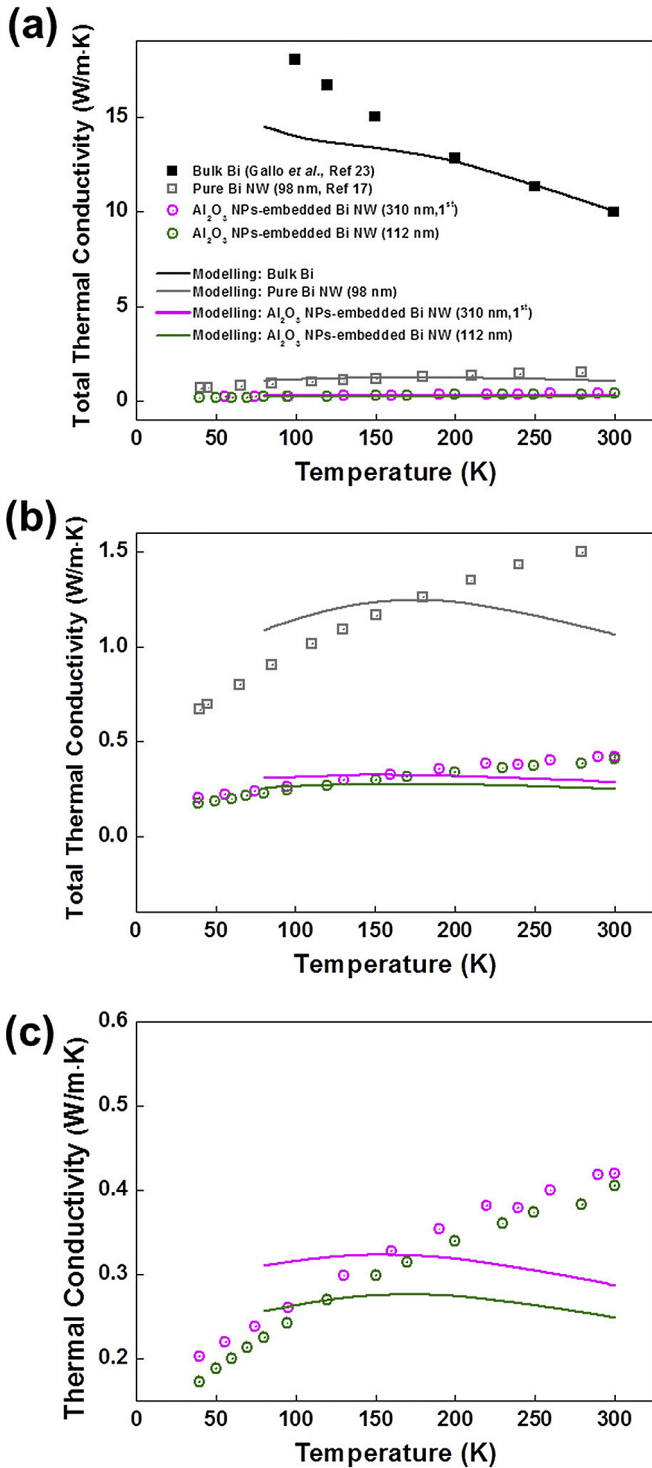


Fig. 7. (a) Experimental (shapes) and calculated (lines) thermal conductivities of bulk Bi, Bi NWs with $d = 98$ nm, and Al_2O_3 NPs-embedded Bi NWs with $d = 310$ and 112 nm. (b) and (c) are the magnified versions of (a) to clearly show that the calculated thermal conductivities satisfactorily describe the measured data.

Consequently, we had to use a C_i that was approximately 5 times greater than that for the Bi NW (98 nm) sample to describe the data in Fig. 7, where C_i is proportional to the strength of the impurity scattering.

Table 1 clearly shows that it is the enhanced impurity scattering owing to Al_2O_3 (in Al_2O_3 NPs-embedded Bi NWs of 310 and 112 nm

in diameter) that drastically reduced their thermal conductivity relative to the pure Bi NW (98 nm) sample. With the relaxation rate becoming dominant in the total relaxation rate owing to the impurity, the difference in the diameters of the two Al_2O_3 NPs-embedded Bi NWs (310 nm and 112 nm) does not result in much difference in the total thermal conductivity. κ_e , κ_h , and κ_{bp} for bulk Bi are calculated based on the transport data provided by Gallo et al. [23]. However, we have assumed that the ratio of $(\kappa_e + \kappa_h + \kappa_{bp})$ to κ_{total} of bulk Bi is maintained even in the NW samples. This is done to minimize the confusion in estimating κ_e , κ_h , and κ_{bp} of the Bi NWs. Moore et al. [20] concluded (after fitting his model to the experimental thermal conductivity of the NWs) that $(\kappa_e + \kappa_h + \kappa_{bp})$ of the NWs was 3–4 times smaller than that of bulk Bi. This is equivalent to our above-mentioned assumption.

4. Conclusion

In summary, Al_2O_3 NPs-embedded single-crystalline Bi NWs were easily synthesized using the OFF-ON method without using any templates. HR-TEM investigation directly reveals that Al_2O_3 nanoparticles were embedded into the single-crystalline Bi nanowires. The temperature-dependent thermal conductivities of individual Al_2O_3 nanoparticles-embedded single-crystalline Bi nanowires were measured directly using suspended micro-devices. The thermal conductivities of the Al_2O_3 nanoparticles-embedded Bi nanowires were found to be extremely low compared with those of pure Bi nanowires of similar diameters. Moreover, the thermal conductivity of the Al_2O_3 nanoparticles-embedded Bi nanowires was not size-dependent, suggesting the dominant phonon scattering mechanism is not phonon-boundary scattering. From the experimental measurements and theoretical calculation, these drastic reduction and unique tendency in the thermal conductivities of Al_2O_3 nanoparticles-embedded Bi nanowires were explained by the combined effect of the phonon-boundary scattering at the surface of nanowires and impurity scattering occurring between the embedded Al_2O_3 nanoparticles and Bi matrix.

Acknowledgment

This work was supported by the National Research Foundation of Korea (NRF) Grant funded by the Government of Korea (MSIP) (2014R1A2A1A10053869).

References

- [1] A.J. Minnich, M.S. Dresselhaus, Z.F. Ren, G. Chen, Bulk nanostructured thermoelectric materials: current research and future prospects, *Energy Environ. Sci.* 2 (2009) 466–479.
- [2] C.J. Vineis, A. Shakouri, A. Majumdar, M.G. Kanatzidis, Nanostructured thermoelectrics: big efficiency gains from small features, *Adv. Mater.* 22 (2010) 3970–3980.
- [3] J. Yang, L. Xi, W. Qiu, L. Wu, X. Shi, L. Chen, J. Yang, W. Zhang, C. Uher, D.J. Singh, On the tuning of electrical and thermal transport in thermoelectrics: an integrated theory–experiment perspective, *NPJ Comput. Mater.* 2 (2016) 15015.
- [4] R.G. Yang, G. Chen, Thermal conductivity modeling of periodic two-dimensional nanocomposites, *Phys. Rev. B* 69 (2004) 195316.
- [5] F. Brochin, B. Lenoir, C. Bellouard, H. Scherrer, Electrical properties of highly disordered bismuth-based composites, *Phys. Rev. B* 63 (2001) 073106.
- [6] A.R. Abramson, W. Kim, S.T. Huxtable, H. Yan, Y. Wu, A. Majumdar, C. Tien, P. Yang, Fabrication and characterization of a nanowire/polymer-based nanocomposite for a prototype thermoelectric device, *J. Microelectromech. Syst.* 13 (2004) 505–513.
- [7] W. Kim, J. Zide, A. Gossard, D. Klenov, S. Stemmer, A. Shakouri, A. Majumdar, Thermal conductivity reduction and thermoelectric figure of merit increase by embedding nanoparticles in crystalline semiconductors, *Phys. Rev. Lett.* 96 (2006) 045901.
- [8] H.L. Ni, X.B. Zhao, T.J. Zhu, X.H. Ji, J.P. Tu, Synthesis and thermoelectric properties of Bi_2Te_3 based nanocomposites, *J. Alloy. Compd.* 397 (2005) 317–321.
- [9] X.A. Fan, J.Y. Yang, Z. Xie, K. Li, W. Zhu, X.K. Duan, C.J. Xiao, Q.Q. Zhang, Bi_2Te_3 hexagonal nanoplates and thermoelectric properties of n-type Bi_2Te_3

- nanocomposites, *J. Phys. D: Appl. Phys.* 40 (2007) 5975–5979.
- [10] L.D. Zhao, B.P. Zhang, J.F. Li, M. Zhou, W.S. Liu, Thermoelectric and mechanical properties of nano-SiC-dispersed Bi₂Te₃ fabricated by mechanical alloying and spark plasma sintering, *J. Alloy. Compd.* 455 (2008) 259–264.
- [11] M. He, C. Stiewe, D. Platzek, G. Karpinski, E. Muller, S.H. Li, M. Toprak, M. Muhammed, Nano ZrO₂/CoSb₃ composites with improved thermoelectric figure of merit, *Nanotechnology* 18 (2007) 235602.
- [12] L.D. Hicks, M.S. Dresselhaus, Thermoelectric figure of merit of a one-dimensional conductor, *Phys. Rev. B* 47 (1993) 16631.
- [13] L.D. Hicks, M.S. Dresselhaus, Effect of quantum-well structures on the thermoelectric figure of merit, *Phys. Rev. B* 47 (1993) 12727.
- [14] A.I. Hochbaum, R. Chen, R.D. Delgado, W. Liang, E.C. Garnett, M. Najarian, A. Majumdar, P. Yang, Enhanced thermoelectric performance of rough silicon nanowires, *Nature* 451 (2008) 163–167.
- [15] D. Li, Y. Wu, P. Kim, P. Yang, A. Majumdar, Thermal conductivity of individual silicon nanowires, *Appl. Phys. Lett.* 83 (2003) 2934.
- [16] J.W. Roh, S.Y. Jang, J.H. Kang, S.H. Lee, J.S. Noh, W.C. Kim, J.H. Park, W.Y. Lee, Size-dependent thermal conductivity of individual single-crystalline PbTe nanowires, *Appl. Phys. Lett.* 96 (2010) 103101.
- [17] J.W. Roh, K. Hippalgaonkar, J.H. Ham, R. Chen, M.Z. Li, P. Ercius, A. Majumdar, W.C. Kim, W.Y. Lee, Observation of anisotropy in thermal conductivity of individual single-crystalline Bi nanowires, *ACS Nano* 5 (2011) 3954–3960.
- [18] W.Y. Shim, J.H. Ham, K.I. Lee, W.Y. Jeung, M. Johnson, W.Y. Lee, On-film formation of Bi nanowires with extraordinary electron mobility, *Nano Lett.* 9 (2009) 18–22.
- [19] J.P. Heremans, C.M. Thrush, D.T. Morelli, M.C. Wu, Thermoelectric power of bismuth nanocomposites, *Phys. Rev. Lett.* 88 (2002) 216801.
- [20] A.L. Moore, M.T. Pettes, F. Zhou, L. Shi, Thermal conductivity suppression in bismuth nanowires, *J. Appl. Phys.* 106 (2009) 034310.
- [21] J.W. Roh, D.H. Ko, J.H. Kang, M.K. Lee, J.H. Lee, C.W. Lee, K.H. Lee, J.S. Noh, W.Y. Lee, Proton irradiation effects on thermal transport in individual single-crystalline Bi nanowires, *Phys. Status Solidi A* 210 (2013) 1438–1441.
- [22] J.H. Kang, J.W. Roh, W.Y. Shim, J.H. Ham, J.S. Noh, W.Y. Lee, Reduction of lattice thermal conductivity in single Bi-Te core/shell nanowires with rough interface, *Adv. Mater.* 23 (2011) 3414–3419.
- [23] C.F. Gallo, B.S. Chandrasekhar, P.H. Sutter, Transport properties of bismuth single crystals, *J. Appl. Phys.* 34 (1963) 144–152.
- [24] A.F. May, G.J. Snyder, Chapter 11. Introduction to modeling thermoelectric transport at high temperatures, in: D.M. Rowe (Ed.), *Materials, Preparation, and Characterization in Thermoelectrics*, CRC Press, 2012, pp. pp.11–1.
- [25] E.S. Toberer, A. Zevalkink, G.J. Snyder, Phonon engineering through crystal chemistry, *J. Mater. Chem.* 21 (2011) 15843–15852.
- [26] J.L. Liu, A. Khitun, K.L. Wang, W.L. Liu, G. Chen, Q.H. Xie, S.G. Thomas, Cross-plane thermal conductivity of self-assembled Ge quantum dot superlattices, *Phys. Rev. B* 67 (2003) 165333.